Incommensurate structure of $GdBaCo_2O_{5+\delta}$ (δ ~0.38)

N. Ishizawa[a1], T. Asaka[a], T. Kudo[a], K. Fukuda[a], N. Abe[b] and T. Arima[b]

[a] *Nagoya Institute of Technology, Japan.*
[b] *Department of Advanced Materials Science, The University of Tokyo, Japan.*

Abstract

The incommensurate structure of the $GdBaCo_2O_{5+\delta}$ (δ ~0.38) paramagnetic phase was studied using the single-crystal X-ray diffraction. The basic structure of the compound is a double-layered perovskite with an alternating layer sequence of $[GdO_\delta]$-$[CoO_2]$-[BaO]-$[CoO_2]$ along the *c* axis. The crystal belongs to the five-dimensional superspace group $P4/mmm(\alpha 00)0000(0\alpha 0)0000$, α = 0.3368(1), with a 1 × 1 × 2-type tetragonal fundamental unit cell of *a* = 3.8934(1) Å and *c* = 7.5267(1) Å. The structure was refined to *R* = 0.028 for all the observed 2216 reflections with $I > 3\sigma(I)$, including 331 main reflections (*R* = 0.017), 1039 observed first-order satellites (*R* = 0.033), and 846 observed second-order satellites (*R* = 0.045). The crystal has oxygen deficiency that occurs only in the $[GdO_\delta]$ layer; however, it causes many positional modulations of the constituting atoms throughout the crystal in association with a valence fluctuation of Co between the divalent and trivalent states. Because the value of α was very close to 1/3, the structure was also investigated using both the commensurately modulated approach and the conventional three-dimensional approach assuming a 3 × 3 × 2 supercell of *P*4/*mmm* symmetry. These approaches successfully reproduced a prime structure of the compound that consists of intersecting CoO_5 pyramidal arrays parallel to *a* and *b* axes. The bond valence sum and the charge neutrality principle suggested that the divalent and trivalent cobalt cations are distributed in an ordered way. The incommensurate approach also indicated the possible presence of a local disorder having a structural similarity with that of a high-temperature modification.

Keywords: Gadolinium Barium Cobaltite, $GdBaCo_2O_{5+\delta}$, Single-crystal X-ray diffraction, Incommensurate structure.

[1] Corresponding author.
E-mail address: ishizawa@nitech.ac.jp (N. Ishizawa)
FAX: +81-572-27-6812

1. Introduction

Double perovskite-type cobalt oxides with the general formula $LnBaCo_2O_{5+\delta}$ (Ln = lanthanide or yttrium) have attracted considerable attention because they exhibit strong correlation between their crystallographic, magnetic, and electrical properties [1, 2]. Moreover, they have recently been proposed as potential candidates for intermediate-temperature solid state oxides fuel cells because of their excellent oxygen transport properties [3-5]. $LnBaCo_2O_{5+\delta}$ has a basic structure with a stacking sequence of $[CoO_2]$-[BaO]-$[CoO_2]$-$[LnO_\delta]$ along the c axis; that is, $c \sim 2a_p$ (a_p: the lattice constant of a simple cubic perovskite cell). In addition to this $1a_p \times 1a_p \times 2a_p$ (abbreviated as 112 hereafter) phase, three types of superstructures related to the oxygen vacancy ordering, $3a_p \times 3a_p \times 2a_p$ (332), $1a_p \times 2a_p \times 2a_p$ (122), and $2a_p \times 2a_p \times 2a_p$ (222) for $\delta \sim 0.44$, 0.5, and 0.75, respectively, have been reported [2, 6-10].

Several studies are reported on the crystal structure of the 122 phase with $\delta \sim 0.5$, because the Co cations are essentially trivalent [8, 11-13]. On the other hand, only a few structural studies of the 332 phase have been reported for $TbBa(Co,Fe)_2O_{5+\delta}$ ($\delta \sim 0.37$) [14] and $YBaCo_2O_{5+\delta}$. ($\delta \sim 0.44$) [15] because of the structural complexity arising from the mixed valence nature of the Co cations. According to the Inorganic Crystal Structure Database (ICSD, 2012/1 version) [16], the structures reported for $GdBaCo_2O_{5+\delta}$ are limited to the 122 phase and no entry can be found for the 332 phase in spite of its important properties bridging the gap between those of the 112 and 122 phases.

Recently, a transmission electron microscope analysis revealed that, under a magnetic field, the 332 phase of $GdBaCo_2O_{5+\delta}$ ($\delta \sim 0.38$) is incommensurate with q_1 = (~1/3, 0, 0) and q_2 = (0, ~1/3, 0) with respect to the fundamental 112 tetragonal cell [17]. In addition, the compound undergoes a phase transition to commensurate 122 at elevated temperatures through different routes depending on the applied magnetic field [17]. This indicates that the transition involves not only the oxygen vacancy ordering but also the spin state of Co.

Herein, we first investigated the temperature dependence of the q vectors of the 332 phase of $GdBaCo_2O_{5+\delta}$ ($\delta \sim 0.38$) using the single-crystal X-ray diffraction under no magnetic field in contrast with the conventional electron microscope study under magnetic fields. The incommensurately modulated structure was then determined at room temperature and compared with those obtained using the commensurate and supercell approaches.

2. Experimental

2.1. Synthesis

Melt-grown single crystals of $GdBaCo_2O_{5+\delta}$ were prepared using the floating-zone method [18]. Powders of Gd_2O_3, Co_3O_4, and $BaCO_3$ were weighed in stoichiometric proportions and then ground. The mixture was calcined at 1173 K for 12 h, pressed into a 6 mmϕ × 100 mm rod, and then sintered at 1473 K for 12 h. A black crystal boule was grown in a flow of air with a feed rate of 3–5 mm/h. Magnetization measurements were performed in a magnetic field of 0.1 T along the *a*-*b* plane using a SQUID magnetometer (Quantum Design, MPMS).

2.2. Diffraction experiment

Data collection was achieved on a spherically shaped crystal (diameter: 90 μm) at room temperature using a Smart ApexII diffractometer with a charge-coupled device (CCD) detector [19]. A monocapillary collimator (diameter: 300 μm) was used to enhance the Mo *K*α X-rays incident on the crystal [20]. In all, 11 series of contiguous frames of data were taken by fixing the CCD at various 2θ positions in the range between −75° and +55°, and sweeping the crystal about ω or ϕ at every 0.3° interval for 30 s. This technique ensured the collection of reciprocal spots up to $2\theta < 90.7°$ with 98% completeness on the assumption of $P\bar{1}$. The total time to collect the entire data set was 53 h. The integrated intensities were obtained from the frame data with concomitant refinements of the q_1 and q_2 vectors, orientation matrix, and various geometrical correction parameters of the diffractometer [19].

The unconstrained *q* vectors, q_1 = [0.33681(3), -0.00004(3), -0.00022(5)] and q_2 = [0.00008(3), 0.33687(3), 0.00025(5)], were obtained through the integration procedure, assuring the further assumptions, $q_1 = (\alpha, 0, 0)$, $q_2 = (0, \alpha, 0)$ and α = 0.3368(1). The tetragonal symmetry was suggested from the unconstrained values of the fundamental cell, *a* = 3.8936 (1), *b* = 3.8930 (1), *c* = 7.5263(11), α = 89.9915(6), β = 90.0089(7), and γ = 89.9978(6), and the consistency among the intensities of equivalent reflections. No systematic extinction of reflections was observed. The superspace group was thus assumed to be $P4/mmm(\alpha 00)0000(0\alpha 0)0000$ with α = 0.3368(1), according to the notation for five-dimensional (5D) superspace groups [21]. The reflection data with five indices *hklmn* ($|m|\leq 1$, $|n|\leq 1$) were then processed using the multi-scan absorption

correction program SADABS [22]. In all, 21501 reflection data were merged into crystallographically-independent 2513 ones with R_{int} = 0.0233, of which 2216 reflections satisfied the criterion $I > 3\sigma(I)$, and were used for further analysis. The crystal data and experimental details are summarized in Table 1. The *hk*0 reciprocal section reconstructed from the frame data is shown in Fig. 1.

The temperature dependence of the *q* vectors and cell dimensions of the 332 phase were also investigated on a different crystal (diameter: 80 μm) in order to confirm the incommensurate nature of the 332 phase. The sample was heated in a hot nitrogen gas stream [23]. A rapid data collection scheme for a total of 3 h in the range $2\theta < 60°$ was employed for each measurement at 296, 323, 353, 383, and 393 K.

2.3. Structure determination and refinements

The structure was determined using the Superflip program [24]. The 5D intensity dataset was first converted to a three-dimensional (3D) dataset in order to solve the 112 average structure, as shown in Fig. 2. The *R* factor converged to 0.0366 for 331 observed fundamental reflections using 18 parameters. The average structure belongs to the space group *P*4/*mmm*, containing six crystallographically independent atoms: Gd1 at 1b (0, 0, 1/2), Ba1 at 1a (0, 0, 0), Co1 at 2h (1/2, 1/2, *z*) with $z \sim 0.254$, O1 at 1c (1/2, 1/2, 0), O2 at 4i (1/2, 0, *z*) with $z \sim 0.299$, and O3 at 1d (1/2, 1/2, 1/2). No significant oxygen deficiency at O1 and O2 was observed in agreement with past studies on $GdBaCo_2O_{5+\delta}$ [2, 3, 8, 9, 13].

The occupational modulation waves for the O3 site and the positional modulation waves for all the atom sites were then examined step-by-step in the 5D superspace. Finally a modulated structure model was obtained as a best compromise between the low *R* factor and the relatively small number of modulation parameters. The incommensurately modulated structure model, “5D-incomm”, converged with *R* = 0.0285 using 67 parameters for the 2216 reflections with $I > 3\sigma(I)$. The composition was determined as $GdBaCo_2O_{5+\delta}$, $\delta = 0.38(1)$ in the final stage of the refinement. No constraint was applied to the site occupation parameter for O3 (O3-Occ) in the least-squares procedure because of the mixed valence nature of Co between divalent and trivalent states.

Because the magnitude of the modulation vectors was close to 1/3, the structure was also examined using a commensurately modulated model, “5D-comm”, and supercell models. In the supercell models, the crystallographically independent atoms are labeled as Gd1a, Gd1b, Gd1c, Ba1a, Ba1b, Ba1c, Co1a, Co1b, Co1c, O1a, O1b, O1c, O2a, O2b,

O2c, O2d, and O3, in order to indicate the relationship with the atom labels given for the fundamental 112 cell. All the models suffered from the treatment of Gd atoms, particularly Gd1a in the supercell models. One supercell approach, “3D-split”, assuming a pair of split-atom sites (Gd1a and Gd1a′ instead of Gd1a), converged with the best *R* factor of 0.0240 using 77 parameters. The site occupancy of Gd1a′ was refined to 5.5(2)% under the constraint that the sum of the Gd1a and Gd1a′ site occupancies is 1. Another supercell approach, “3D-anharm”, assuming the 3rd order anharmonic atomic displacement parameters (ADPs) for Gd1a, also converged with $R = 0.0269$ using 78 parameters. The commensurately modulated approach, “5D-comm”, assuming the 3rd order ADP for Gd1, converged with $R = 0.0279$ using the minimum number of 63 parameters. The results of the refinements based on the four models are summarized in Table 2, and the interatomic distances and bond valence sums (BVSs) [25] are compared in Table 3.

All the calculations were completed using the Jana2006 program [26]. The extinction was corrected using the Becker and Coppens formalism [27]. Atomic scattering factors [28] and dispersion factors [29] were taken from the International Tables for Crystallography Vol. C. The structure was plotted using the Vesta program [30]. Changes in various structural properties on the *t*-*u* section were plotted using the Graph-R program [31]. For the BVS calculation, it was assumed that $b_o = 2.065$ Å for Gd^{3+} [32], 2.285 Å for Ba^{2+} [33], and 1.7 Å for Co^{3+} [32], with a constant *B* value of 0.37 Å. The final structural data are given in the supplementary tables and CIF files.

3. Results and discussion

3.1. Physical properties

Figure 3 shows magnetization of the $GdBaCo_2O_{5+\delta}$ crystal as a function of temperature. As the temperature decreases below 350 K, the magnetization steeply increases below ~290 K, and then decreases around 230 K with additional small bending around 270 K and 250 K. This behavior is qualitatively similar to those of $LnBaCo_2O_{5+\delta}$ (*Ln* = Nd, Gd, or Tb) reported in previous studies, where the anomalies at ~290 K and ~230 K are interpreted as transitions from a paramagnetic state to ferromagnetic [34, 35] or antiferromagnetic ones [36, 37], and to antiferromagnetic [34, 35] or spin-state ordering ones [36, 37], respectively. Therefore, our diffraction experiments were carried out for the compound in the paramagnetic state.

Figure 4 shows the temperature dependence of α and the reduced dimensions of the fundamental cell. The α value of the *q* vectors increased rapidly when the temperature approached ~393 K, at which the commensurate 122 phase commenced to appear and coexisted with the incommensurate 332 phase. The magnitude of the *q* vector of the 332 phase is so close to the commensurate value of 1/3 at room temperature that the incommensurate nature of the 332 phase tends to be overlooked. The present study confirmed quantitatively the incommensurate nature of the 332 phase under zero magnetic fields for the first time through measurements of the temperature dependence of the *q* vectors using X-ray diffraction.

3.2. Atomic displacements

The atomic displacements of the constituent atoms from those in the average structure are plotted on the *t*-*u* section (Fig. 5). The most conspicuous displacement occurs for Gd1 along *a* (Gd1-Δ*ax*) with a maximum magnitude of 0.45 Å. The next largest displacement occurs for O2 along *c* (O2-Δ*cz*) with a magnitude of 0.34 Å, followed by O3 along *a* (O3-Δ*ax*) at 0.26 Å, and O1 along *a* (O1-Δ*ax*) at 0.16 Å. The other displacements of Ba1 along *a* (Ba1-Δ*ax*) and Co1 along *c* (Co1-Δ*cz*) are relatively small on the order of 0.05 Å at a maximum, and that of O2 along *a* (O2-Δ*ax*) is the smallest (maximum of 0.02 Å).

The atomic displacements can be summarized in such a way that the O3 deficiency triggers large positional modulations of the atoms in the GdO layer at $z = 1/2$, which then invoke the modulation of the *z* coordinates of the atoms in the adjacent CoO layers at $z \sim 1/4$ and 3/4, and finally affects the *x* coordinates of O1 in the second-neighbor BaO layers at $z = 0$ and 1. Accordingly, the positional modulation waves encompass the entire crystal to greater or lesser degrees.

3.3. Oxygen deficiency

The O3-Occ on the *t*-*u* section is shown in Fig. 6 with three typical approximants at two extrema: A (1/3, 1/3), where O3-Occ ~ 0; B (5/6, 5/6), where O3-Occ ~ 1; and a saddle point F (5/6, 1/3). Because the *q* vectors are close to 1/3, any topography on the *t*-*u* section is pseudo-periodic at 1/3 intervals along *t* and *u*. For example, the approximant at A′ (0, 0) is nearly the same as that at A (1/3, 1/3) after an appropriate shift of the origin. The same is true for the relationships between B′ (1/6, 1/6) and B (5/6, 5/6) and between F′ (1/6, 0) and F (5/6, 1/3).

The A-type approximant has linear arrays of the corner-shared O3-vacant CoO_5 pyramids along *a* and *b* directions (Fig. 6). The O3-Occ is minimized at the intersection of the pyramidal arrays. The F-type approximant also has pyramidal arrays similar to those in A, but they are aligned in a parallel way along *a* or *b*, and do not intersect with each other (Fig. 6). The B-type approximant has no such clear CoO_5 pyramidal arrays.

Modulation of the O3-Occ on the layer $z = 0.5$ for an extended area containing 50 × 50 fundamental unit cells is depicted in Fig. 7. Oxygen-deficient pyramidal arrays running parallel to *a* or *b* are shown with a blue background. The regions A, F, and B have structures similar to the three typical approximants given in Fig. 6, respectively.

The pyramidal arrays intersecting at right angles are clearly visible in the region A, forming an ideal 3 × 3 supercell-like arrangement. The O3-Occ in the arrays parallel to *a* and *b* gradually increase with increasing *y* and *x* toward 50, respectively, except those at the intersection. As a result, the 3 × 3 nature in the region A attenuates in the regions F_1 and F_2, and 1 × 3 and 3 × 1 natures are favored instead, respectively. Region B is also affected by the Occ variation, and the 3 × 3 nature is barely managed with every three O3 sites fully occupied and the oxygen-deficient O3 sites capping the $Co(II)O_5$ pyramid (section 3.5).

3.4. Modulation of Gd and its surroundings

Changes in the Gd1-O3 distances on the *t*-*u* section are shown in Fig. 8 with a relevant 332 approximant at G, where the largest displacement of Gd1 from the average position occurs. The five Gd1 and four O3 atoms form a tightly-bound planar cluster with the Gd1–O3 bonds less than 2.7 Å on the $z = 1/2$ layer. This cluster formation suggests that the encircled Gd cation pair (Fig. 8), facing each other through two nearly vacant O3 sites in the CoO_5 pyramidal arrays, tends to distance themselves to mitigate the electrostatic repulsion.

A similar behavior is observed for the Gd pair in the approximant at M (not depicted), where the largest displacement of O3 from the average position occurs on the $z = 1/2$ layer (Fig. 5). The closeness of the two extrema (G (8/12, 0) and M (7/12, 0)) indicates a high correlation between the Gd1 and O3 displacements. Thus, the O3-Occ plays an important role in determining not only the Gd1 positions but also the O2 locations: Gd1 tends to stay away from the O3 vacancies and O2 behaves oppositely (sections 3.5 and 3.6).

3.5. Modulation of the Co polyhedra

The Co cations are surrounded by O atoms either in octahedral or square pyramidal coordination units depending on O3-Occ. Changes in the Co1-O1, Co1-O2, and Co1-O3 bond-lengths and Co-BVS on the *t*-*u* section are shown in Fig. 9 with approximants at the representative extrema or saddle points. The changes in Co-BVS show a similar topography to O3-Occ (Fig. 6), suggesting a high correlation between them. The changes in Co1-O1, however, are governed mainly by Co1-Δ*cz* (Fig. 5) because of mild changes in O1-Δ*ax* (Fig. 5). Moreover, the changes in Co1-O1 (Fig. 9) and Co1-Δ*cz* (Fig. 5) have a reverse topography compared to those of Co-BVS (Fig. 9) and O3-Occ (Fig. 6). This result indicates that Co slightly moves upward in the *z* direction when its oxidation state is lowered along with a concomitant decrease in O3-Occ. An extreme occurs at A (1/3, 1/3) where O3 becomes nearly empty and the Co-BVS is minimized close to +2. As shown in Figs. 6 and 7, this situation occurs only for the CoO_5 pyramid located at the intersection of two pyramidal arrays, indicating an ordered distribution of the divalent Co(II) in the crystal. The upward *z* shift of O2 is presumably induced by the local charge compensation around the empty O3 site in the GdO_{δ} layer.

If we write ^{Py}Co(II) for Co(II) at the intersection of pyramidal arrays, ^{Py}Co(III) for the other Co in pyramidal arrays, and ^{Oc}Co(III) for Co in the O3-deficient octahedra outside of the pyramidal arrays, the ideal composition of the region A can be expressed as $GdBa[^{Py}Co(II)_{1/9}\,^{Py}Co(III)_{4/9}{}^{Oc}Co(III)_{4/9}]_2O_5{}^{Oc}O_{\delta}$. Here, the symbol $^{Oc}O_{\delta}$ indicates that the O3 atom ordering occurs in the GdO layer such that all the δ O3 atoms exist only at the ^{Oc}Co(III) octahedra. The charge neutrality principle for this composition constrains δ = 7/18 (~ 0.389) in good agreement with the experimentally determined value of 0.38(1) for the present crystal. Conclusively, the present 332 crystal has a charge-ordered nature regarding the Co valency.

3.6. Modulation of the BaO layer

The BaO layer contains no oxygen deficiency. Because the displacement modulation waves of Ba1 and O1 are relatively small in magnitude, the bond distance changes modestly between 2.65 and 2.90 Å. On the other hand, the displacive modulation waves of O2 are larger than those of O1 in magnitude, resulting in a larger variation in Ba1-O2 bond distances between 3.08 (at K and U) and 2.66 Å (at L), as shown in Fig. 10. Because the variation in Ba1-Δ*ax* and O2-Δ*ax* are very small (Fig. 5), the topography of the Ba1-O2 distance on the *t*-*u* section becomes similar to that of O2-Δ*cz* in Fig. 5.

It should be noted that the upward *z* shift of the O2 atoms in association with the decrease in O3-Occ leads to a longer Ba1-O2 distance. Figure 5 shows that the topography of O1-Δ*ax* has a reverse relationship with O3-Δ*ax* along *t*, and the same holds true for O1-Δ*by* along *u* (not depicted). These relationships indicate that the displacements of O1 and O3 occur in opposite directions in each layer perpendicular to *c* in order to preserve the linearity of the O1-Co-O3 linkage, as exemplified in the S and T approximants (Fig. 10). An orbital mixing between Co and O should thus be considered for further study.

3.7. Comparison of the supercell and commensurately modulated models

Figure 11 compares the 332 supercell model "3D-split" assuming a split pair of Gd1a and Gd1a′, the another 332 supercell model "3D-anharm" assuming the 3rd order anharmonic vibration for Gd1a instead of the spilt pair, and the commensurately-modulated model "5D-comm" assuming the 3rd order anharmonic vibration for Gd1. There is no significant difference between the "3D-split" and "3D-anharm" models except for the local environment surrounding the split pair in the former. The Gd1a′ in the "3D-split" model forms a characteristic coordination polyhedron with two short (2.27 Å), six middle (2.47Å ×4 and 2.54 Å ×2), and four long bonds (2.76 Å ×2, 2.91 Å ×2), in contrast with a relatively regular Gd1a polyhedron surrounded by twelve O in the range 2.43–2.63 Å in the "3D-anharm" model. The "3D-anharm" model gives way to the "3D-split" model in that the former fails to describe the existence of very short (2.27 Å) and long (2.91 Å) Gd1a′–O bonds. On the other hand, these extreme bonds are identified in the "5D-incomm" model (2.27~3.08Å), but not in the "5D-comm" model (2.41~2.86 Å). These different results indicate that the anharmonic ADP adopted in the "3D-anham" and "5D-comm" models may not cope with the abrupt and relatively large displacement of the Gd atoms.

The distribution of O3-Occ becomes simplified in the order, "5D-incomm" < "5D-comm" < "3D-split" (or "3D-anharm"). No significant O3-Occ was detected for any of the pyramidal arrays in either of the 332 supercell models ("3D-anharm" and "3D-split"). The "5D-comm" model showed no significant O3-Occ at the intersection of the pyramidal arrays, but a small portion of O was observed on the other O3 sites of the arrays (Fig. 11). The "5D-incomm" model, on the other hand, showed a small portion of O even at the intersection of the Co pyramidal arrays (A′ in Fig. 6), which seems to be unavoidable when sinusoidal approximations are employed for Occ modulations in the

5D superspace.

The 5D-commensurate and the 3D-supercell approaches provide structures similar to those depicted in region A (Fig. 7), indicating that the A-type approximant is the prime structure of the 332 phase. On the other hand, this 3 × 3 character attenuates in regions distant from A in the incommensurate analysis. The F-type approximant has a similarity to the 122 phase in which the pyramidal arrays do not intersect, but align in parallel [6]. Considering that the 332 phase undergoes a phase transition via an intermediate state to 122 at elevated temperatures [17], the F-type structural disorder in 332 at room temperature can be regarded as an embryo of the 122 high-temperature phase. The B-type structural disorder could then embody some features of the intermediate state during the 332–122 transition.

As mentioned in section 3.5, the ideal composition of the charge-ordered 332 phase can be expressed as $GdBa[^{Py}Co(II)_{1/9}\,^{Py}Co(III)_{4/9}\,^{Oc}Co(III)_{4/9}]_2O_5\,^{Oc}O_{\delta}$, where $\delta = 7/18$. Let us consider a case in which the 332 phase exists over a certain range of δ where the charge ordering is slightly broken off, but all the O3 sites in the pyramidal arrays are still empty. The composition can then be expressed as $GdBa[Co(II)_{1/2-\delta}Co(III)_{1/2+\delta}]_2O_5\,^{Oc}O_{\delta}$, and the mean O3-Occ of the octahedral units outside of the pyramidal arrays becomes $(9/4) \times \delta$.

Figure 12 shows the fraction of Co(II) and Co(III) and the mean O3-Occ of the octahedra in the compound as a function of δ ($0 < \delta < 1/2$). If $\delta = 7/18$ (~0.389), the mean O3-Occ of octahedra is 7/8, indicating that the O3 sites of octahedra are not yet completely filled. The mean O3-Occ of octahedra becomes 1 at $\delta = 8/18$ (~0.444); herein, the GdO_{δ} layer attains a perfect ordering of the oxygen vacancies. This δ value (8/18) can be considered as the upper limit of the O concentration in the 332 phase. It is worthy to emphasize that the ideal O concentration ($\delta = 7/18$) for the Co charge ordering in 332 neither coincides with that for the perfect ordering of oxygen vacancies in 332 ($\delta = 8/18$), nor that for the 122 high-temperature phase expressed as $GdBa[^{Py}Co(III)_{1/2}\,^{Oc}Co(III)_{1/2}]_2O_{5+\delta}$ ($\delta = 9/18$). The incommensurate nature of the present crystal seems to stem from these misfits of composition.

Conclusion

The incommensurate nature of a 332-type $GdBaCo_2O_{5+\delta}$ (δ ~0.38) crystal was identified through the measurement of the temperature dependence of the q vectors using single-crystal X-ray diffraction under zero magnetic fields. The room-temperature

structure was studied through various approaches; 1) an incommensurately modulated, 2) a commensurately modulated, 3) a conventional supercell assuming anharmonic atomic displacement parameters for part of the Gd atoms, and 4) a conventional supercell assuming a split-atom model for these Gd atoms.

Crystals have the oxygen deficiency in the [GdO_{δ}] layer, which causes positional modulations of the constituting atoms in association with a valence fluctuation of Co between divalent and trivalent states. The absence of any O3 atom in the GdO layer invokes displacements not only the neighboring Gd atoms but also the Co and O2 atoms surrounding the O3 vacancy.

Broadly speaking, the 332 supercell models succeeded in describing a clear-cut image of the A-type structure, which typically occurs in the compound, consisting of CoO_5 pyramidal arrays running along the *a* and *b* axes. The bond valence sum and the charge-neutrality principle of the composition indicated that the Co atoms are divalent only at the intersection of the pyramidal arrays and trivalent at the other sites, i.e., the Co charge is essentially ordered in the present crystal.

On the other hand, the incommensurate approach revealed not only the A-type but also a range of alternatives, some of which showed a structural similarity to the high-temperature orthorhombic 122 modification at the point where the CoO_5 pyramidal arrays run parallel only along one direction. This type of intrinsic local disorder in the room-temperature 332 phase could provide important information about the phase transition mechanisms of the compound at elevated temperatures. A study on the in-situ single-crystal X-ray diffraction of the 332–122 phase transition of $GdBaCo_2O_{5+\delta}$ (δ ~0.38) is in progress.

Acknowledgements

The authors are grateful to Dr Vaclav Petricek, Institute of Physics, Academy of Science, Czech Republic, for his valuable comments and calculations, and Dr Terutoshi Sakakura, Institute of Multidisciplinary Research for Advanced Materials, Tohoku University, Japan, for supplying us a Python script for data conversion. This work was supported by JSPS KAKENHI Grant number 22360272.

Appendix A. Supplementary material

Supplementary data associated with this article can be found in the online version at doi:xxxxxx/j.jjjc.yyyyyyyyyyyy.

References

[1] Y. Moritomo, M. Takeo, X.J. Liu, T. Akimoto, A. Nakamura, *Phys. Rev. B: Condens. Matter Mater. Phys.* 58 (1998) R13334-R13337.

[2] A. Maignan, C. Martin, D. Pelloquin, N. Nguyen, B. Raveau, *J. Solid State Chem.* 142 (1999) 247-260.

[3] A.A. Taskin, A.N. Lavrov, Y. Ando, *Appl. Phys. Lett.* 86 (2005) 091910-3.

[4] A. Tarancón, A. Morata, G. Dezanneau, S.J. Skinner, J.A. Kilner, S. Estradé, F. Hernández-Ramírez, F. Peiró, J.R. Morante, *J. Power Sources* 174 (2007) 255-263.

[5] J. Peña-Martínez, A. Tarancón, D. Marrero-López, J.C. Ruiz-Morales, and P. Núñez, *Fuel Cells (Weinheim, Ger.)* 8 (2008) 351-359.

[6] W. Zhou, C.T. Lin, W.Y. Liang, *Adv Mater.* 5 (1993) 735-738.

[7] D. Akahoshi, Y. Ueda, *J. Solid State Chem.* 156 (2001) 355-363.

[8] C. Frontera, J.L. García-Muñoz, A. Llobet, M.A.G. Aranda, *Phys. Rev. B: Condens. Matter Mater. Phys.* 65 (2002) 180405.

[9] C. Frontera, J.L. García-Muñoz, A.E. Carrillo, C. Ritter, D. Martín y Marero, A. Caneiro, *Phys. Rev. B: Condens. Matter Mater. Phys.* 70 (2004) 184428.

[10] C. Frontera, J.L. García-Muñoz, A.E. Carrillo, M.A.G. Aranda, I. Margiolaki, A. Caneiro, *Physical Review B* 74 (2006) 054406.

[11] Y. Moritomo, T. Akimoto, M. Takeo, A. Machida, E. Nishibori, M. Takata, M. Sakata, K. Ohoyama, A. Nakamura, *Phys. Rev. B: Condens. Matter Mater. Phys.* 61 (2000) R13325-R13328.

[12] S. Roy, M. Khan, Y.Q. Guo, J. Craig, N. Ali, *Phys. Rev. B: Condens. Matter Mater. Phys.* 65 (2002) 064437.

[13] L. Lo Presti, M. Allieta, M. Scavini, P. Ghigna, L. Loconte, V. Scagnoli, M. Brunelli, *Phys. Rev. B: Condens. Matter Mater. Phys.* 84 (2011) 104107.

[14] D.D. Khalyavin, A.M. Balagurov, A.I. Beskrovnyi, I.O. Troyanchuk, A.P. Sazonov, E.V. Tsipis, V.V. Kharton, *J. Solid State Chem.* 177 (2004) 2068-2072.

[15] D.D. Khalyavin, D.N. Argyriou, U. Amann, A.A. Yaremchenko, V.V. Kharton, *Phys. Rev. B: Condens. Matter Mater. Phys.* 75 (2007) 134407.

[16] ICSD: Inorganic Crystal Structure Database, Fachinformationszentrum Karlsruhe, Germany, 2012.

[17] T. Asaka, T. Kudo, K. Fukuda, Y. Matsui, T. Arima, N. Ishizawa, Aperiodic 2012, Cairns, 2012.

[18] T. Saito, T. Arima, Y. Okimoto, Y. Tokura, *J. Phys. Soc. Jpn.* 69 (2000) 3525.
[19] Bruker, SAINT and Smart Apex II, Bruker AXS Inc., Madison, Wiskonsin, 2007.
[20] B.B. He, U. Preckwinkel *Adv. X-Ray Anal.* 45 (2002) 332-337.
[21] H.T. Stokes, B.J. Campbell, S. van Smaalen, *Acta Crystallogr., Sect. A: Found. Crystallogr.* 67 (2011) 45-55.
[22] G.M. Sheldrick, in: G. SADABS. Program for Empirical Absorption. Correction of Area Detector Data. University of Gottingen, (Ed.), 1996.
[23] N. Ishizawa, S. Kondo, H. Hibino, S. Igarashi, M. Nakamura, R. Saho, *Annual Report of Ceramics Research Laboratory 2006, Nagoya Institute of Technology* 6 (2007) 12-18.
[24] L. Palatinus, G. Chapuis, *J. Appl. Cryst.* 40 (2007) 786-790.
[25] I.D. Brown, *The Chemical Bond in Inorganic Chemistry: The Bond Valence Model*. Oxford University Press, 2002.
[26] V. Petricek, M. Dusek, L. Palatinus, Institute of Physics, Praha, Czech Republic., 2006.
[27] P.J. Becker, P. Coppens, *Acta Crystallogr., Sect. A: Found. Crystallogr.* 30 (1974) 129-147.
[28] P.J. Brown, A.G. Fox, E.N. Maslen, M.A. O'Keefe, B.T.M. Willis, in: E. Prince, (Ed.), International Tables for Crystallography Vol. C, Kluwer Academic Publishers, London, 2004, pp. 559-595.
[29] D.C. Creagh, in: E. Prince, (Ed.), International Tables for Crystallography Vol. C, Kluwer Academic Publishers, London, 2004, pp. 241-258.
[30] K. Momma, F. Izumi, *J. Appl. Crystallogr.* 44 (2011) 1272-1276.
[31] T. Itoh, Graph-R ver. 2.29, http://www.graph-project.com/, 2012.
[32] N.E. Brese, M. O'Keeffe, *Acta Crystallogr., Sect. B: Struct. Sci.* 47 (1991) 192-197.
[33] I.D. Brown, D. Altermatt, *Acta Crystallogr., Sect. B: Struct. Sci.* 41 (1985) 244-247.
[34] A.A. Taskin, A.N. Lavrov, Y. Ando, *Phys. Rev. B: Condens. Matter Mater. Phys.* 71 (2005) 134414.
[35] D.-q. Liao, M.R. Lees, G. Balakrishnan, D.M. Paul, *J. Phys.: Conference Series* 200 (2010) 012104.
[36] F. Fauth, E. Suard, V. Caignaert, I. Mirebeau, *Phys. Rev. B* 66 (2002) 184421.
[37] V.P. Plakhty, Y.P. Chernenkov, S.N. Barilo, A. Podlesnyak, E. Pomjakushina, E.V. Moskvin, S.V. Gavrilov, *Phys. Rev. B* 71 (2005) 214407.

Figure captions

Fig. 1. The *hk*0 reciprocal section reconstructed from the frame data. Indices provided are based on the 112 fundamental cell.

Fig. 2. Average structure of $GdBaCo_2O_{5+\delta}$ (δ ~0.38) in the 112 fundamental cell.

Fig. 3. Temperature dependence of magnetization for the $GdBaCo_2O_{5+\delta}$ crystal in a 0.1 T magnetic field along the *a*-*b* plane.

Fig. 4. The α value of the *q* vectors and reduced cell dimensions, *a* and *c*/2, of $GdBaCo_2O_{5+\delta}$ (δ ~0.38) as a function of temperature.

Fig. 5. Atomic displacements (Å) from their average positions on the *t*-*u* section: Gd1-Δ*ax*, Ba1-Δ*ax*, Co1-Δ*ax*, Co1-Δ*cz*, O1-Δ*ax*, O2-Δ*ax*, O2-Δ*cz*, and O3-Δ*ax*. All the maps except for Gd1-Δ*ax* have the same color bar chart between ±0.34 Å for comparison. The Gd1-Δ*ax* map has a larger scale between ±0.45 Å with a different corresponding color bar chart.

Fig. 6. Changes in O3-Occ on the *t*-*u* section and the approximant structures ($-0.2 < x < 3.2$, $-0.2 < y < 3.2$, $-0.1 < z < 0.6$) at A′ (0, 0), F′ (1/6, 0) and B′ (1/6, 1/6). The CoO_5 pyramidal array containing rather deficient O3 is depicted on the blue background in the *c* axis projection. The O3-Occ is represented in the red sector of the atom sphere. See Fig. 1 for the other color schemes.

Fig. 7. Distribution of O3-Occ in the approximant ($0 \le x \le 50$, $0 \le y \le 50$, and $0.4 \le z \le 0.6$). One fundamental cell contains one O3 at its center. The CoO_5 pyramidal array is depicted on the blue background with the tone attenuated with increasing O3-Occ. The regions A, B, and F contain the typical structures given in Fig. 5, respectively.

Fig. 8. Changes in the Gd1–O3 bond distances on the *t*-*u* section and arrangement of the GdO_δ layer in the 3 × 3 approximants ($-1.2 < x < 2.2$, $-1.2 < y < 2.2$, $z = 0.5$) at G (8/12, 0). The Gd1–O3 bonds are drawn when their lengths are shorter than 2.72 Å. The black solid line indicates the fundamental lattice viewed along the *c* axis. The pyramidal arrays beneath the GdO_δ layer are colored in blue. Atom color schemes

are the same as those in Fig. 1.

Fig. 9. Changes in the Co-O bond length and the local structures ($-0.2 < x < 1.2$, $-0.2 < y < 0.2$, $-0.1 < z < 0.6$) at selected extrema or saddle points on the *t*-*u* sections. Arrows indicate relatively large O2 atom displacements along *c*. The approximants in the bottom line are rotated 5° about *c* such that all of the O2 atoms of the Co polyhedra can be seen. Atom color schemes are the same as those in Fig. 1.

Fig. 10. Changes in the Ba1–O1 and Ba1–O2 bond lengths and the local structures ($-0.2 < x < 1.2$, $-0.2 < y < 1.2$, $-0.1 < z < 0.6$) at the selected extremes S (11/12, 1/12), T (8/12, 8/12), K (4/12, 0), U (9/12, 6/12), and L (10/12, 0). The two-colored Ba–O1 and Ba–O2 bonds are those used for the *t*-*u* plot. The structures at K, U, and L are rotated 5° about *c* such that all the O2 atoms of the Co polyhedra can be seen. The dashed line across Co is just for viewing convenience to observe how the O2 atoms displace along *c*. Atom color schemes are the same as those in Fig. 1.

Fig. 11. The *c*-axis projection of (a) the 332 supercell model with a split pair of Gd1a and Gd1a′ (“3D-split”), (b) the 332 supercell model assuming an anharmonic vibration for Gd1a (“3D-anharm”), and (c) the commensurately modulated model assuming an anharmonic vibration for Gd1 (“5D-comm”). Because the labeling scheme for the two supercells (a) and (b) is essentially the same, the Gd (purple) and Co (blue) atoms are labeled in (a), and the Ba (green) and O (red) atoms are labeled in (b) in order to avoid congestion. The atom labeling for the ‘5D-comm’ model follows Fig. 1.

Fig. 12. The fraction of Co(II) and Co(III), and the mean O3-Occ of the octahedral units outside of the pyramidal arrays as a function of δ in the 332 phase, assuming that O3-Occ is completely zero in the pyramidal arrays, as in the 3D supercell models.

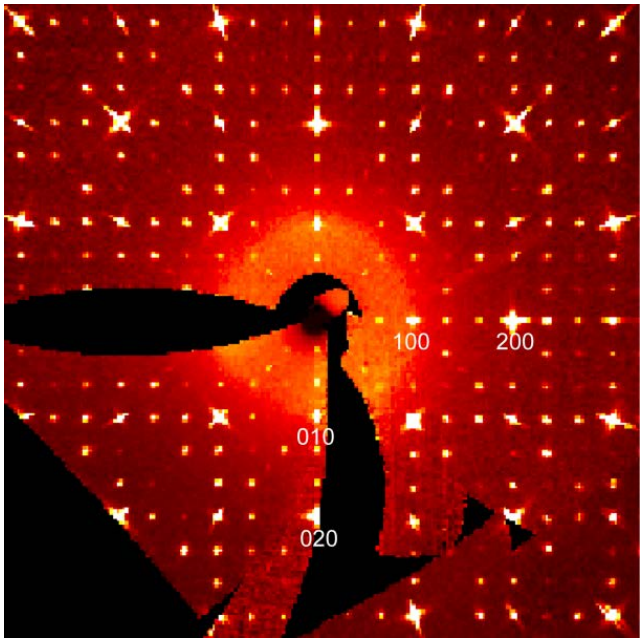

Fig. 1

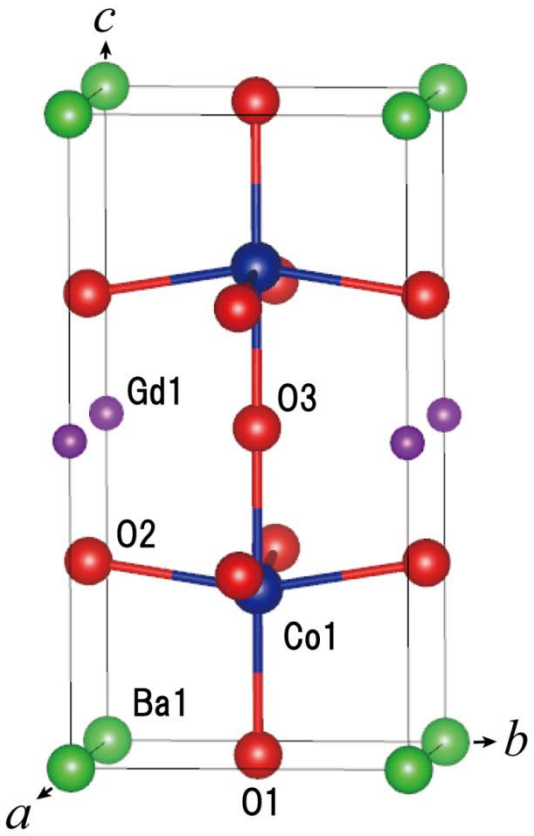

Fig. 2.

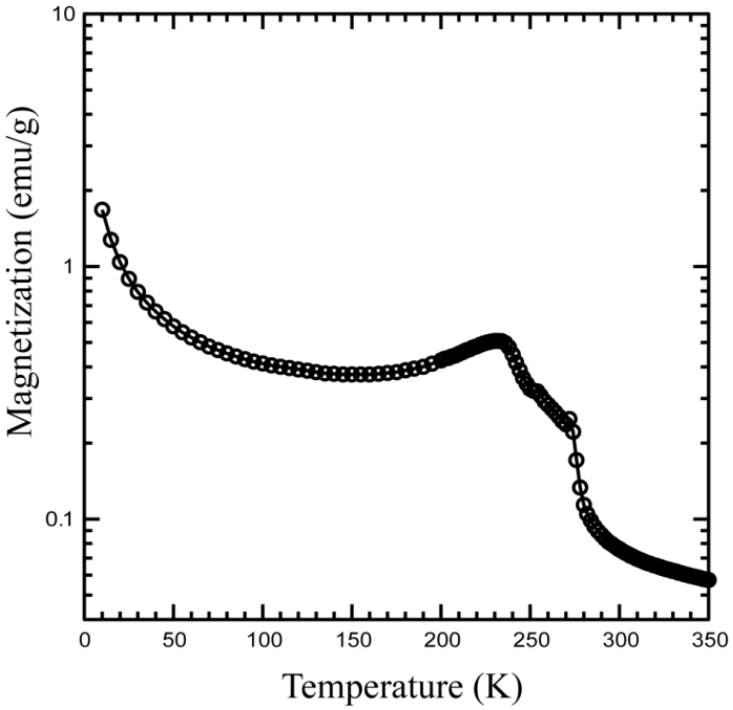
Magnetization (emu/g)
10
1
0.1
0
50
100
150
200
250
300
350
Temperature (K)

Fig. 3.

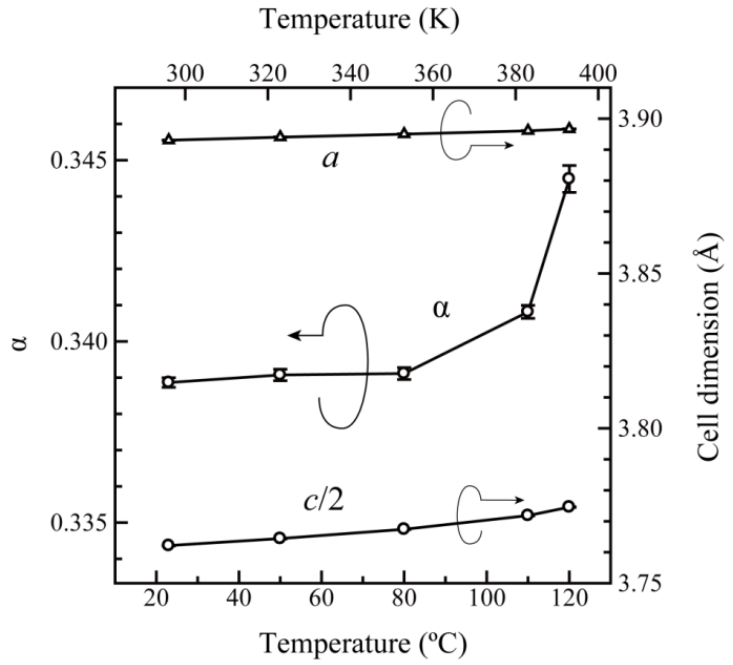
Temperature (K)
300
320
340
360
380
400
0.345
0.340
0.335
α
a
α
c/2
3.90
3.85
3.80
3.75
Cell dimension (Å)
20
40
60
80
100
120
Temperature (ºC)

Fig. 4.

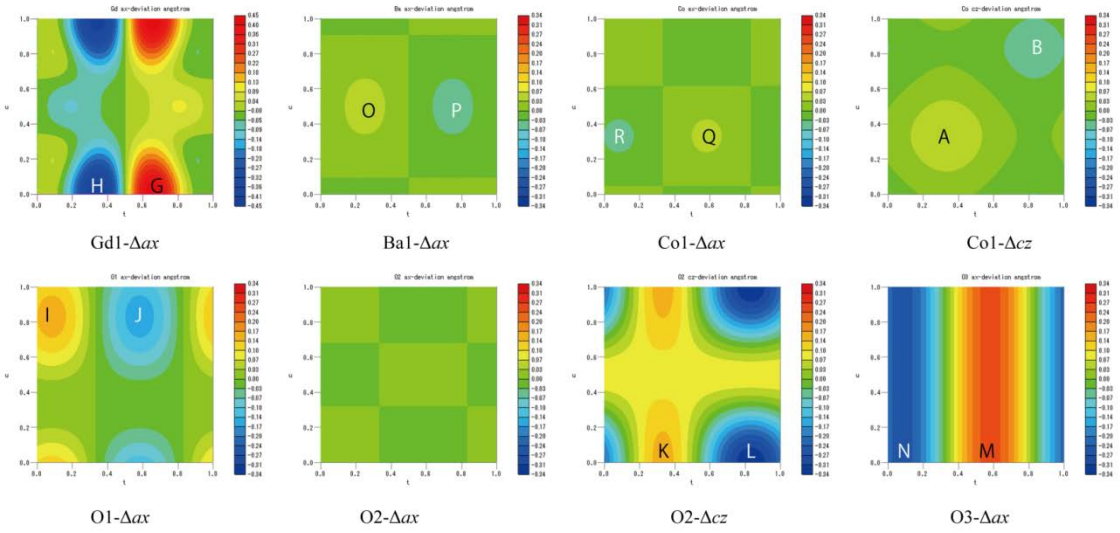
H
G
O
P
R
Q
B
A
I
J
K
L
N
M
Gd1-Δax
Ba1-Δax
Co1-Δax
Co1-Δcz
O1-Δax
O2-Δax
O2-Δcz
O3-Δax

Fig. 5

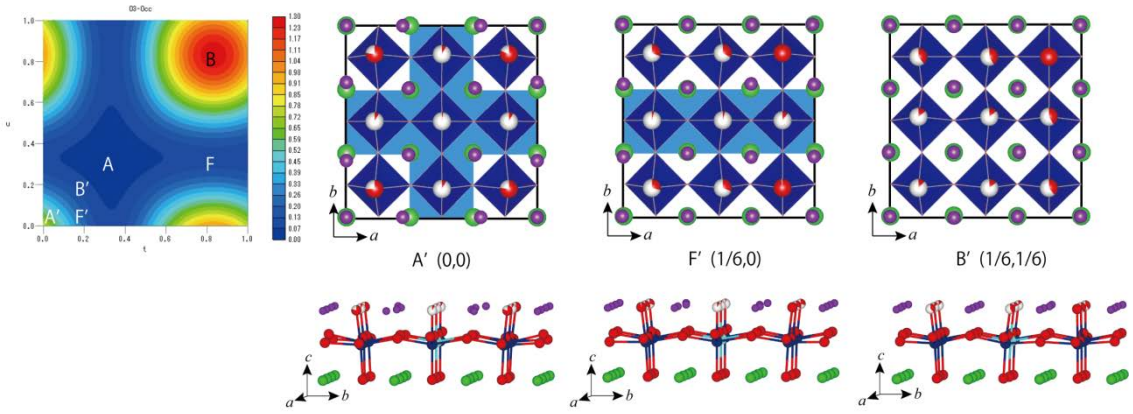
B
A
F
B′
A′
F′
A′ (0,0)
F′ (1/6,0)
B′ (1/6,1/6)
a
b
c

Fig. 6.

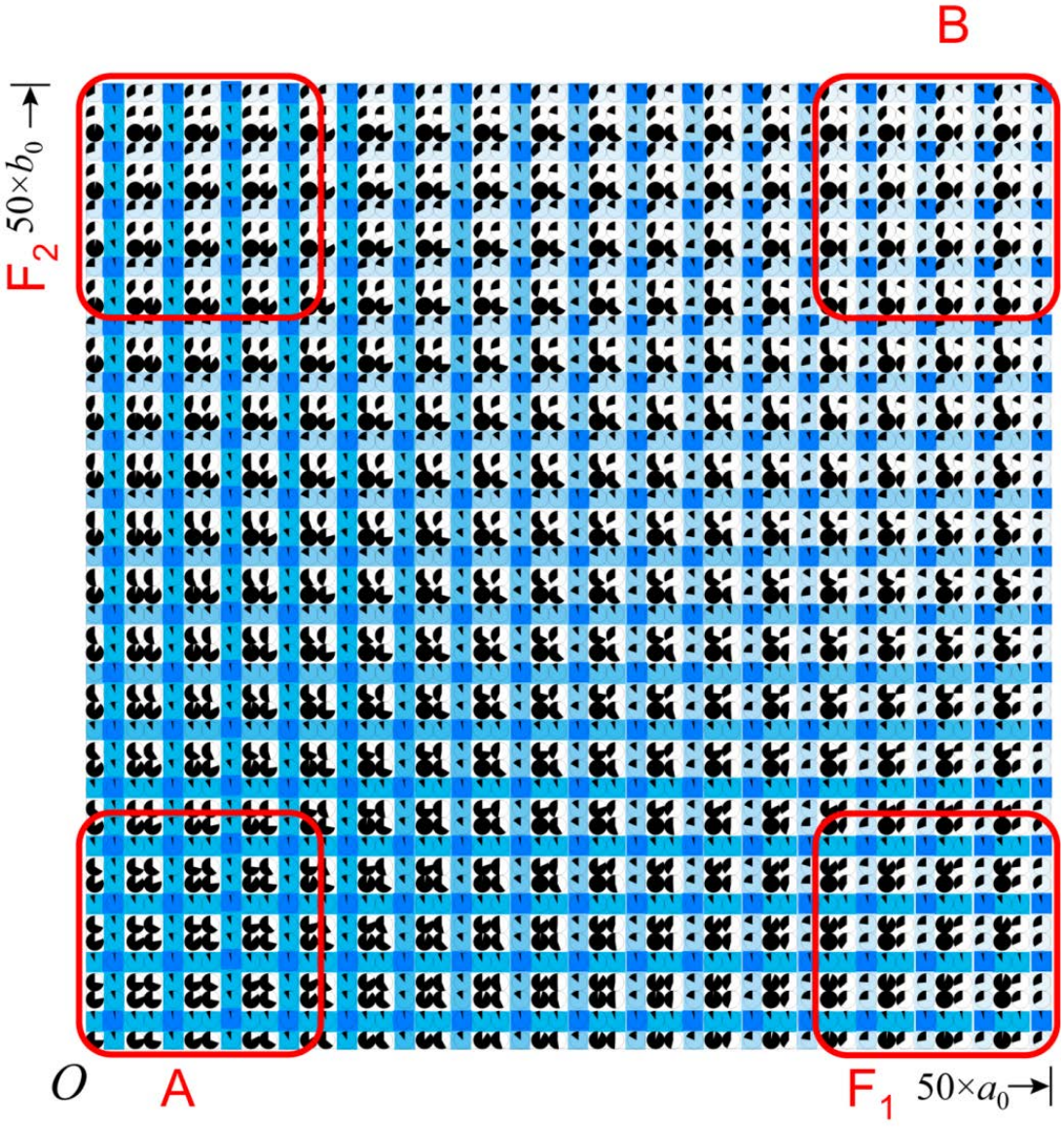

Fig. 7.

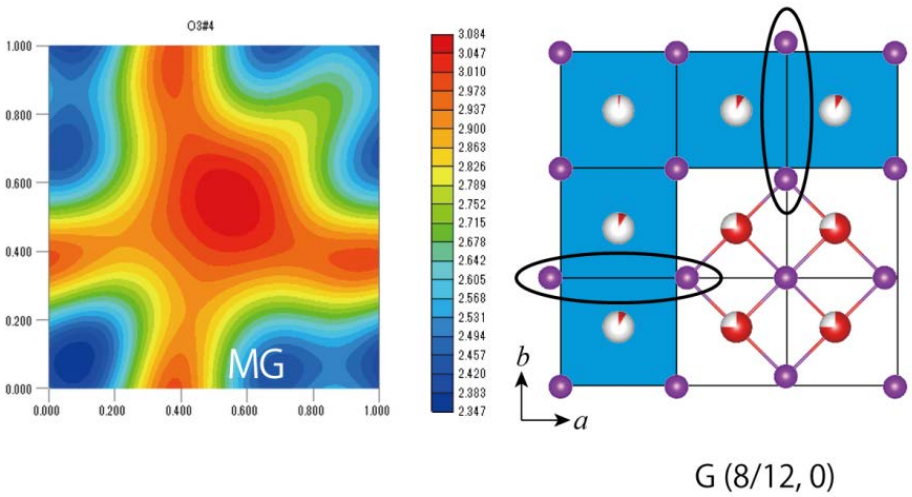
O3#4
MG
b
a
G (8/12, 0)

Fig.8.

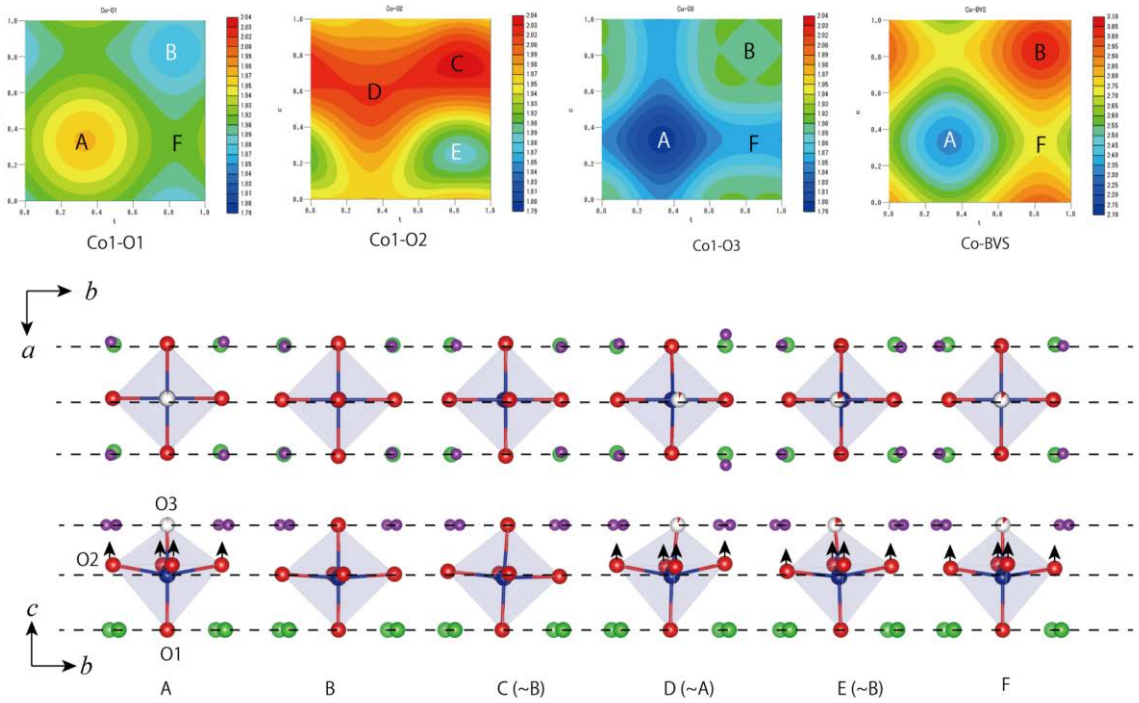
A
B
C
D
E
F
Co1-O1
Co1-O2
Co1-O3
Co-BVS
b
a
O3
O2
O1
c
b
A
B
C (~B)
D (~A)
E (~B)
F

Fig. 9.

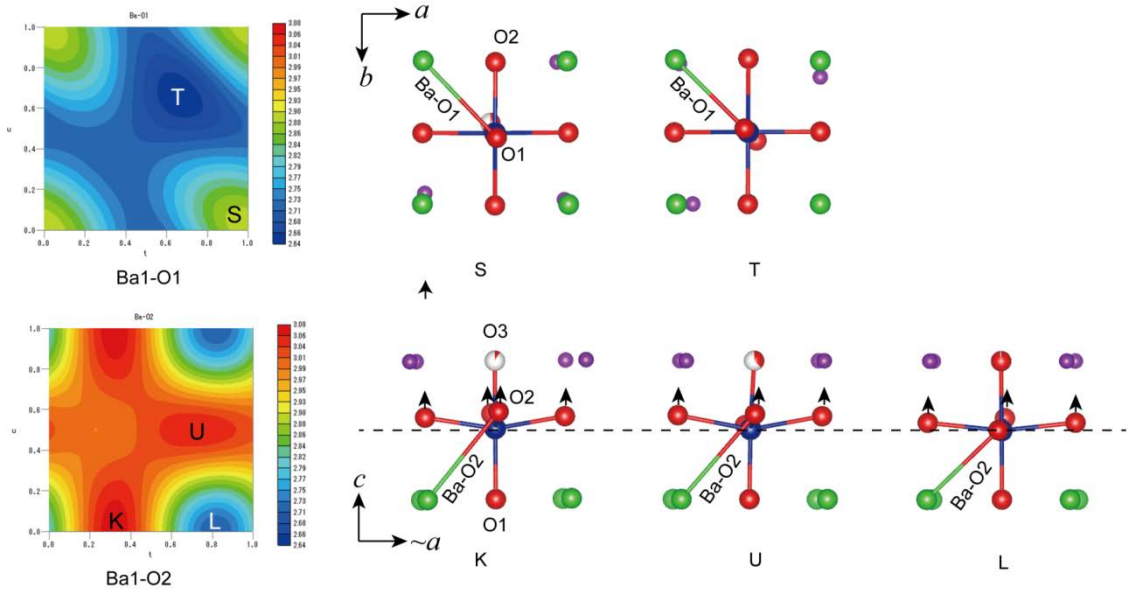
T
S
Ba1-O1
U
K
L
Ba1-O2
a
b
O2
Ba-O1
O1
S
T
O3
c
~a
Ba-O2
K
U
L

Fig. 10.

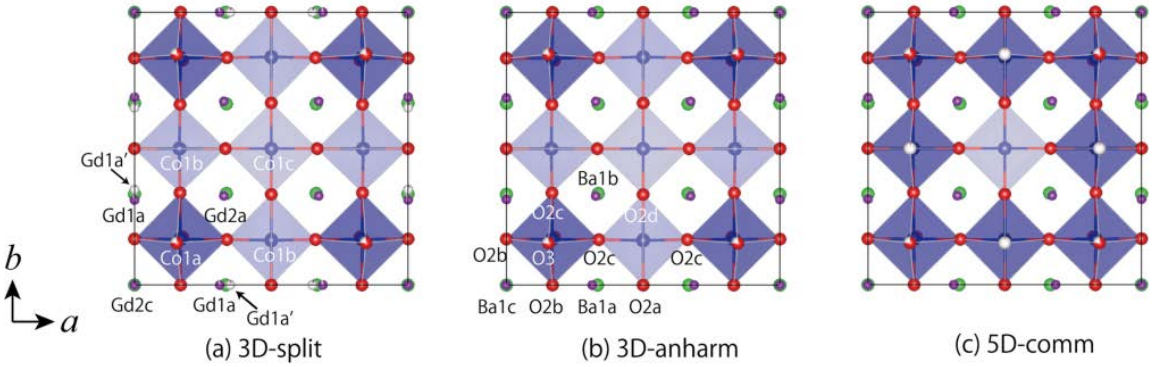
Gd1a′
Co1b
Co1c
Gd1a
Gd2a
Co1a
Co1b
Gd2c
Gd1a
Gd1a′
b
a
(a) 3D-split
Ba1b
O2c
O2d
O2b
O3
O2c
O2c
Ba1c
O2b
Ba1a
O2a
(b) 3D-anharm
(c) 5D-comm

Fig. 11.

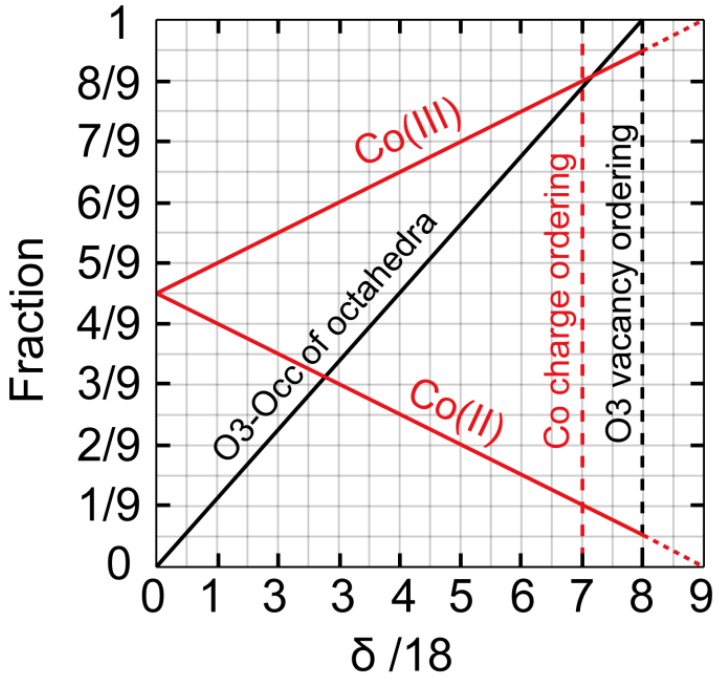
Fraction
1
8/9
7/9
6/9
5/9
4/9
3/9
2/9
1/9
0
0 1 3 3 4 5 6 7 8 9
δ /18
Co(III)
O3-Occ of octahedra
Co(II)
Co charge ordering
O3 vacancy ordering

Fig. 12.

Table 1

Crystal data and experimental.

chemical formula	$Gd_1Ba_1Co_2O_{5.377}$
chemical fw	498.1
temperature (K)	293
cell setting	tetragonal
superspace group	$P4/mmm(\alpha 00)0000(0\alpha 0)0000$ with $\alpha = 0.3368(1)$
a (Å)	3.8934(1)
c (Å)	7.5267(1)
vol (Å ^{3})	114.094(4)
no. of formula units (Z)	1
Dx (Mg m^{-3})	7.247
modulation wave vectors	q_1 = (0.3368(1) , 0, 0)
	q_2 = (0, 0.3368(1), 0)
crystal form	sphere
crystal size (mm)	0.09
crystal color	black
diffractometer	Bruker Smart ApexII CCD diffractometer
radiation type	Mo $K\alpha$
wavelength (Å)	0.71073
absorption correction type	multiscan
absorption coeff (μ) (mm^{-1})	29.926
range of h, k, l, m, and n	$-6 \le h \le 8$
	$-8 \le k \le 8$
	$-15 \le l \le 14$
	$-1 \le m \le 1$
	$-1 \le n \le 1$
no. of measured reflections	21501
no. of unique reflections	2513
no. of observed reflections	2216
no. of observed main reflections	331
no. of observed satellites	
for ± (1,0) ± (0,1)	1039
for ± (1,1) ± (-1,1)	846
criterion for observed reflections	$I > 3\sigma(I)$
R_{int} for equivalents	0.0233

Table 2

Summary of the four refinement models.

	3D-split	3D-anharm	5D-comm	5D-incomm
model	3 × 3 × 2 supercell assuming split-atom model for Gd1a (into Gd1a and Gd1a')	3 × 3 × 2 supercell assuming anharmonic ADP for Gd1a	commensurately modulated assuming anharmonic ADP for Gd1	incommensurately modulated assuming harmonic ADP for Gd1
modulation vectors			q_1= (1/3,0,0) q_2 = (0,1/3,0)	q_1 = (0.3368,0,0), q_2 = (0,0.3368,0)
a (Å)	11.6802(1)	11.6802(1)	3.8934(1)	3.8934(1)
c (Å)	7.5267(1)	7.5267(1)	7.5267(1)	7.5267(1)
V (Å^3)	1026.85(2)	1026.85(2)	114.094(4)	114.094(4)
independent Ga atoms	Gd1a, Gd1b, Gd1c, Gd1a′	Gd1a, Gd1b, Gd1c	Gd1	Gd1
independent Ba atoms	Ba1a, Ba1b, Ba1c	Ba1a, Ba1b, Ba1c	Ba1	Ba1
independent Co atoms	Co1a, Co1b, Co1c	Co1a, Co1b, Co1c	Co1	Co1
independent O atoms	O1a, O1b, O1c O2a, O2b, O2c, O2d, O3	O1a, O1b, O1c O2a, O2b, O2c, O2d, O3	O1, O2, O3	O1, O2, O3
anharmonic ADP		Gd1a	Gd1	
harmonic ADP	all except for O3	all except for O3 & Gd1a	all except for O3 & Gd1	all except for O3
isotropic ADP	O3	O3	O3	O3
S	2.51	2.69	2.79	2.9
no. of refined params.	77	78	63	67
R/*R*w for all reflns. (obs)	2.40/3.93 (2216)	2.69/4.21 (2216)	2.79/4.29 (2216)	2.85/4.55 (2216)
R/*R*w for main reflns. (obs)			2.16/3.94 (331)	1.73/3.16 (331)
R/*R*w for 1st ord. satel. (obs)			2.62/3.96 (1039)	3.33/4.73 (1039)
R/*R*w for 2nd ord. satel. (obs)			4.66/5.68 (846)	4.55/5.34 (846)

Table 3

Interatomic distances (Å) and bond valence sums (valence unit) in the four refinement models.

	split	anharm		comm	incomm
Gd1a–O2a (×2)	2.626(2)	2.606(2)	Gd1–O2 (×8)		
Gd1a–O2b (×2)	2.432(3)	2.450(3)	average	2.497(3)	2.499(5)
Gd1a–O2c (×4)	2.4859(16)	2.4835(18)	min	2.414(3)	2.273(6)
Gd1a–O3 (×2)	2.574(3)	2.592(3)	max	2.650(3)	2.761(9)
average	2.521	2.523			
			Gd1–O3 (×4)		
Gd1a′–O2a (×2)	2.268(6)		average	2.743(2)	2.745(7)
Gd1a′–O2b (×2)	2.754(6)		min	2.538(3)	2.354(9)
Gd1a′–O2c (×4)	2.4702(17)		max	2.862(3)	3.084(7)
Gd1a′–O3 (×2)	2.907(6)				
average	2.574				
Gd1b–O2c (×4)	2.4121(16)	2.4121(18)			
Gd1b–O2d (×4)	2.4820(14)	2.4821(15)			
Gd1b–O3	2.857(3)	2.859(3)			
average	2.493	2.493			
Gd1c–O2b (×8)	2.646(3)	2.645(3)			
Gd1c–O3 (×4)	2.541(3)	2.539(3)			
average	2.611	2.61			
			Gd1-BVS		
Gd1a-BVS	2.841(6)	2.820(6)	average	2.827(7)	2.919(15)
Gd1a'-BVS	2.957(13)		min	2.472(6)	2.661(13)
Gd1b-BVS	2.949(4)	2.948(5)	max	2.938(7)	3.181(18)
Gd1c-BVS	2.487(5)	2.493(6)			
Ba1a–O1a (×2)	2.759(2)	2.760(2)	Ba1–O1 (×4)		
Ba1a–O1b (×2)	2.755(2)	2.755(3)	average	2.754(3)	2.759(3)
Ba1a–O2a (×2)	3.038(3)	3.037(3)	min	2.647(3)	2.648(3)
Ba1a–O2b (×2)	2.770(3)	2.771(3)	max	2.900(3)	2.899(3)
Ba1a–O2c (×4)	2.9731(17)	2.9731(18)			
average	2.878	2.878	Ba1–O2 (×8)		
			average	2.951(3)	2.951(3)
Ba1b–O1a (×2)	2.749(2)	2.749(2)	min	2.766(3)	2.709(5)
Ba1b–O1b	2.647(2)	2.647(3)	max	3.038(5)	3.073(5)
Ba1b–O1c	2.71209(17)	2.71234(18)			
Ba1b–O2c (×4)	2.9930(17)	2.9923(18)			
Ba1b–O2d (×4)	3.0154(19)	3.015(2)			
average	2.908	2.907			
Ba1c–O1b (×4)	2.900(2)	2.900(3)			
Ba1c–O2b (×8)	2.804(3)	2.804(3)			
average	2.836	2.836			
			Ba1-BVS		
Ba1a-BVS	2.539(5)	2.538(5)	average	2.511(6)	2.496(7)
Ba1b-BVS	2.408(4)	2.409(4)	min	2.413(6)	2.390(7)
Ba1c-BVS	2.725(6)	2.729(6)	max	2.753(7)	2.691(7)
Co1a–O1b	1.8918(4)	1.8918(4)	Co1–O1 (×1)		
Co1a–O2b (×2)	1.9578(3)	1.9574(3)	average	1.9136(7)	1.9124(7)

Co1a–O2c (×2)	2.0268(15)	2.0269(16)	min	1.8920(7)	1.8672(13)
Co1a–O3.	1.8896(5)	1.8898(5)	max	1.9692(13)	1.9667(13)
average	1.958	1.958			
			Co1–O2 (×4)		
Co1b–O1a	1.9215(4)	1.9216(5)	average	1.973(2)	1.974(2)
Co1b–O2a	1.9557(9)	1.9561(10)	min	1.919(2)	1.884(4)
Co1b–O2c (×2)	1.9191(15)	1.9192(16)	max	2.026(2)	2.034(4)
Co1b–O2d	2.010(2)	2.009(2)			
average	1.945	1.945	Co1–O3 (×1)		
			average	1.8680(7)	1.8704(9)
Co1c–O1c	1.9690(9)	1.9695(10)	min	1.8462(6)	1.7970(13)
Co1c–O2d (×4)	1.991(2)	1.992(2)	max	1.8898(7)	1.9042(8)
average	1.987	1.988			
			Co1-BVS		
Co1a-BVS	2.867(3)	2.865(3)	average	2.681(6)	2.711(6)
Co1b-BVS	2.589(4)	2.590(5)	min	2.307(7)	2.335(8)
Co1c-BVS	2.304(6)	2.301(6)	max	2.865(5)	3.045(8)